



Evaporation with the formation of chains of liquid bridges

Chen Chen, Pierre Joseph, Sandrine Geoffroy, Marc Prat, Paul Duru

► To cite this version:

Chen Chen, Pierre Joseph, Sandrine Geoffroy, Marc Prat, Paul Duru. Evaporation with the formation of chains of liquid bridges. *Journal of Fluid Mechanics*, 2018, 837, pp.703-728. 10.1017/jfm.2017.827 . hal-01701199

HAL Id: hal-01701199

<https://laas.hal.science/hal-01701199>

Submitted on 5 Feb 2018

HAL is a multi-disciplinary open access archive for the deposit and dissemination of scientific research documents, whether they are published or not. The documents may come from teaching and research institutions in France or abroad, or from public or private research centers.

L'archive ouverte pluridisciplinaire **HAL**, est destinée au dépôt et à la diffusion de documents scientifiques de niveau recherche, publiés ou non, émanant des établissements d'enseignement et de recherche français ou étrangers, des laboratoires publics ou privés.

Evaporation with formation of liquid bridges chains

C. Chen^{1†}, P. Joseph², S. Geoffroy³, M. Prat¹, and P. Duru^{1‡}

¹Institut de Mécanique des Fluides de Toulouse (IMFT) - Université de Toulouse, CNRS-INPT-UPS, Toulouse, France

²LAAS-CNRS, Université de Toulouse, CNRS, Toulouse, France

³Laboratoire Matériaux et Durabilité des Constructions (LMDC) -Université de Toulouse, UPS-INSA, Toulouse, France

(Received xx; revised xx; accepted xx)

The objective of the present work is to study the drying of a quasi-2D model porous medium, thereafter called micromodel, initially filled with a pure liquid. The micromodel consists of cylinders measuring $50\mu\text{m}$ in both height and diameter, radially arranged as a set of neighbouring spirals and sandwiched between two horizontal, flat plates. As drying proceeds, air invades the pore space and elongated liquid films trapped by capillary forces form along the spirals. These films consist of “chains” of liquid bridges connecting neighbouring cylinders. They provide an hydraulic connectivity between the central, bulk liquid cluster and the external rim of the cylinders pattern, where evaporation is taking place during a first constant evaporation-rate drying stage. The first goal of the present paper is to describe experimentally the phase distribution during drying, notably the liquid films evolution, which controls the evaporation kinetics (e.g. the depinning of the films from the external rim signs the end of the constant evaporation rate period). Then, a visco-capillary model for the drying process is presented. It is based on numerical simulations of a liquid film capillary shape and of the viscous flow within a film. The model shows a reasonably good agreement with the experimental data. Thus, the present study is a step towards direct modelling of the films effect on the drying of more complex porous media (e.g. packing of beads) and should be of interest for multiphase flow applications in porous media, involving transport within liquid films.

Key words:

1. Introduction

Many multiphase flow applications in porous media, e.g. drying or oil recovery processes, involve fluid transport within liquid films present owing to capillary effects in the pore space. As the main application behind the work presented in this paper is drying (Van Brakel 1980; Scherer 1990), let’s detail the liquid films effect on the drying kinetics of a porous medium. Starting with a porous medium saturated with a volatile liquid, a first drying stage displaying a constant evaporation rate (CRP) is usually observed. During this first period, the liquid is transported across a partially-saturated region to the

† Present address: Guangdong Key Laboratory for Biomedical Measurements and Ultrasound Imaging, Department of Biomedical Engineering, Shenzhen University, China

‡ Email address for correspondence: duru@imft.fr

sample surface. In the partially-saturated region, the hydraulic connectivity is ensured by a network of liquid-filled pores and thick films in partially-filled pores. In fact, as the liquid evaporates, “thick” liquid films (by contrast with thin liquid films adsorbed by surface forces on solid matrix) remain trapped by capillary forces within the pore space, on the anfractuosités, cracks, contacts between constituting particles, etc...depending on the considered porous medium. As saturation in the partially-saturated region decreases, liquid transport to the evaporative surface eventually takes place within a network of connected liquid films, under the action of the capillary pressure gradient induced by the meniscus curvature variation along the films (capillary pumping). The evaporation rate in the CRP is controlled by external environmental conditions (relative humidity and temperature of external air, presence of a external flow or not, etc...). The existence of such a partially-saturated region has been demonstrated by the use of 3D imaging techniques such as MRI (Shahidzadeh-Bonn *et al.* 2007) and X-ray tomography, the latter having a high enough spatial resolution to image the 3D liquid films network that ensures the hydraulic connectivity from the liquid-saturated region to the evaporative surface (see e.g. Kohout *et al.* 2006; Shokri *et al.* 2010; Yang *et al.* 2015). Note that such a liquid films network is also a key element when considering the mechanical properties (e.g. cohesion energy) of wet granular media (Scheel *et al.* 2008a).

In a second drying period, the evaporation rate decreases rather sharply and this is attributed to the progressive formation of a dry region below the porous medium evaporative surface (falling rate period, FRP). The transition from the CRP to this second period occurs when the partially-saturated zone has reached a maximal extent, which results from a balance between capillary pumping, which drives the flow up to the evaporative surface and the opposing effects of gravitational force (hydrostatic pressure drop) and viscous dissipation (pressure drop induced by the evaporation-driven flow taking place within the films). Again, 3D imaging techniques have shown that the fall of the drying rate is correlated with the appearance of dry patches at the sample surface, with a large enough extent to have an impact on drying rate. Finally, a third drying stage called receding front period (RFP) is sometimes introduced. It is characterized by the existence of a fully dry region below the sample surface. While during the FRP some evaporation still takes place at the sample surface, the evaporation takes place inside the porous structure during the RFP. As a result, the drying rate decrease is different in the FRP and in the RFP.

Since pioneering works on drying (Lewis 1921; Sherwood 1929*a,b*; Ceaglske & Hougen 1937), describing the different drying regimes and the transition between them has been the subject of many studies, based on scaling analysis (Tsimpanogiannis *et al.* 1999; Lehmann *et al.* 2008; Coussot 2000) and pore network or continuous modelling (see e.g. Prat 2007, 2011; Yiotis *et al.* 2003, 2004). From an experimental perspective, the study of drying also benefited from the use of model systems, geometrically much simpler than a “real” porous medium such as packing of beads confined in a Hele-Shaw cell (Shaw 1987) or microfabricated quasi-2D model porous media, thereafter called micromodels (Laurindo & Prat 1998). Note, however, that such studies are relatively few, especially when compared to other “classical” porous-media-related research topics, where micromodels have become a standard tool since the pioneering works of Lenormand *et al.* (1988), see for instance recent works on supercritical CO₂ trapping (Hu *et al.* 2017), oil recovery (Lacey *et al.* 2017), rheology (Machado *et al.* 2016) or immiscible fluid displacement (Jung *et al.* 2016). Regarding drying, recent advances came from a simpler model system that retains the liquid film ingredient: capillary tubes with polygonal cross-sections (Chauvet *et al.* 2009; Keita *et al.* 2016). The drying of capillary tubes with square cross-sections was thoroughly studied by Chauvet *et al.* (2009, 2010*a,b*) and was shown to

display a succession of drying regimes similar to that documented for a porous medium and summed up above. In fact, while the tube liquid saturation decreases, elongated films remain trapped along the tube internal corners and transport the liquid from the liquid-saturated region to the tube opened end, where evaporation occurs. Consequently, a constant evaporation rate period is first observed. Depinning of the films from the tube top causes a sudden decrease of the evaporation rate (FRP) before a third period, characterized by the development of a dry region in the tube top part (RFP). Modelling the flow in the corner films and using experimental data for the evaporation rate, the authors predicted the films maximal extent as a function of Bond and capillary numbers, in good agreement with the experimental data. They notably highlighted the importance of the tube internal corners roundedness through its key impact on the viscous resistance to the evaporation-induced flow (Chauvet *et al.* 2010*b*). Such an understanding of the transition between the drying regimes, gained from a simple model system, has been used in an ad-hoc fashion to describe the drying of beads packing (Yiotis *et al.* 2012*b,a*) and inspired more realistic pore network modelling techniques (Vorhauer *et al.* 2015).

However, the elongated corner liquid films found in polygonal cross-section capillary tubes have a well-described and simple interface shape and it might be expected that the square capillary tube analogy has some limits when it comes to explaining/predicting the transport properties of liquid films of much complex shape as those imaged in 3D packings of beads. In fact, Scheel *et al.* (2008*a,b*), using close inspection of 3D X-ray tomography images, have shown that the liquid clusters present in a packing of spherical beads can be classified at low liquid content into several generic class of morphologies: liquid bridge between two particles, between three particles (“trimers”), four particles (“pentamers”) and so on... The coalescence of such basic units at higher liquid content leads to a complex 3D liquid “lace” with long range hydraulic connectivity within the resulting liquid cluster (Scheel *et al.* 2008*a*) which certainly provides a good idea of the 3D liquid films networks obtained in drying and at play during the CRP. Interestingly, Cejas *et al.* (2016) recently reported some experiment on the drying of a single column of spherical beads, confined in a capillary tube. They related the experimentally observed drying kinetics to the topology of the films network, which displays a transition between a funicular and a pendular regimes, respectively with and without long range connectivity, depending on the granular packing configuration within the tube.

In this paper, the goal is to study drying in a model system displaying liquid films with shapes more complex than those found in straight, square capillary tubes, as a step towards real 3D films networks such as those described above and to study the relationship between the drying kinetics and the liquid films topology and hydraulic conductivity. To that end, we study the drying of a micromodel consisting of cylindrical pillars arranged in a phyllotaxy-inspired, spiral pattern (Douady & Couder 1992), and sandwiched between two horizontal flat plates. As discussed in Chen *et al.* (2017), such a design enables the formation of elongated liquid films consisting of “chains” of liquid bridges between cylinders, as the drying of the initially saturating liquid occurs, which provide long range connectivity within this model porous medium. Thus, the liquid bridges between two constitutive particles of the solid matrix (i.e. the cylinders) in the micromodel used in the present study are conceptually akin to those found between spherical particles in beads packing, and imaged by Scheel *et al.* (2008*a,b*).

After presenting in Section 2 the experimental set-up and techniques used in the present study, the main experimental results are exposed in Section 3. We show that the drying kinetics follows the usual picture presented briefly above, with a transition between a constant rate period and a falling rate period controlled by the extent of the liquid films in the micromodel. Also, the invasion of the model porous medium under study

can be described by a succession of two different kinds of events: invasion of a pore or modification of the liquid films topology (film extent and film external end location within the micromodel). In Section 4, the focus is the modelling of the drying invasion pattern, using the measured drying rates as an input. Gravity effect can be neglected in the present study (small Bond numbers). Then, the liquid films dynamics results from a balance between capillary and viscous effects. The former depend on the local pore-space geometry and play a key role in the pore invasion process and the presence of liquid bridges in between neighbouring cylinders, which control partly the films extent via a transition between a funicular regime, where liquid bridges “connect” several cylinders along a spiral, and a pendular regime, where such a connection is lost. Some of these aspects are studied using interfacial shapes simulations with the Surface Evolver software (Brakke 1992). The viscous effects are related to the evaporation-induced flow in the elongated films, which induces pressure variations within the liquid films. The viscous dissipation modelling requires direct numerical simulations of the Stokes flow within the liquid bridges. Finally, we develop a visco-capillary model that is in a reasonable agreement with the data obtained, as far as the drying invasion pattern is concerned. Therefore, the present work can be seen as a step in the study of transport in networks of liquid films of complex shape.

2. Experimental setup and techniques

2.1. Micromodel design and microfabrication

Figure 1 shows the full micromodel pattern: 661 cylinders of diameter d_c are arranged along 28 spirals and sandwiched between two plates, separated by a height h . In Figure 1, the cylinders along a given spiral are marked out by an integer number between 1 and 24, with the number 1 for the most external cylinder. The center-to-center distances between two neighbouring cylinders along a given spiral, $w_{//}$, and between a cylinder and its closest neighbour in the adjacent spiral (in the counter-clockwise direction), w_{\perp} , are shown in Figure 2. In this paper, we present results obtained on micromodels designed with $h = d_c = 50 \mu\text{m}$. Note that in order to validate the image processing algorithm used to measure the amount of liquid within a micromodel against data obtained using a balance (see §2.3), we also had to use a larger micromodel, with $d_c = 500 \mu\text{m}$ and $h = 525 \mu\text{m}$.

The microfabrication protocol combines the classical photo-lithography, exposure, bake and development steps with the commonly used epoxy-based SU8 photo-resist as a material. It is detailed in Chen (2016) and we only highlight here some of its key features. First, it is important to note that for the large micromodel, the glass bottom plate is covered by a $10 \mu\text{m}$ -thick SU8 layer, prior to the cylinders realization. The glass top plate is also covered by a $10 \mu\text{m}$ -thick SU8 layer before bonding. Thus, all the surfaces in contact with the liquid are made of SU8, see Figure 1. Second, the protocol for the small system differs from the one used for the large system on one major point: the top plate only consists of a $20 \mu\text{m}$ dry epoxy film (DF1020 negative photo-resist) which is laminated on top of the bottom part of the micromodel (after the pattern of cylinders has been completed). The circular shape of the top plate is obtained following a photo-lithography/exposure/bake/development procedure during which a good alignment of the top plate is ensured (whereas it is done manually in the large micromodel). Characterization of the micromodels bottom plates after microfabrication by optical profilometry and SEM ensured that the designed dimensions were well reproduced, typically within a few microns.

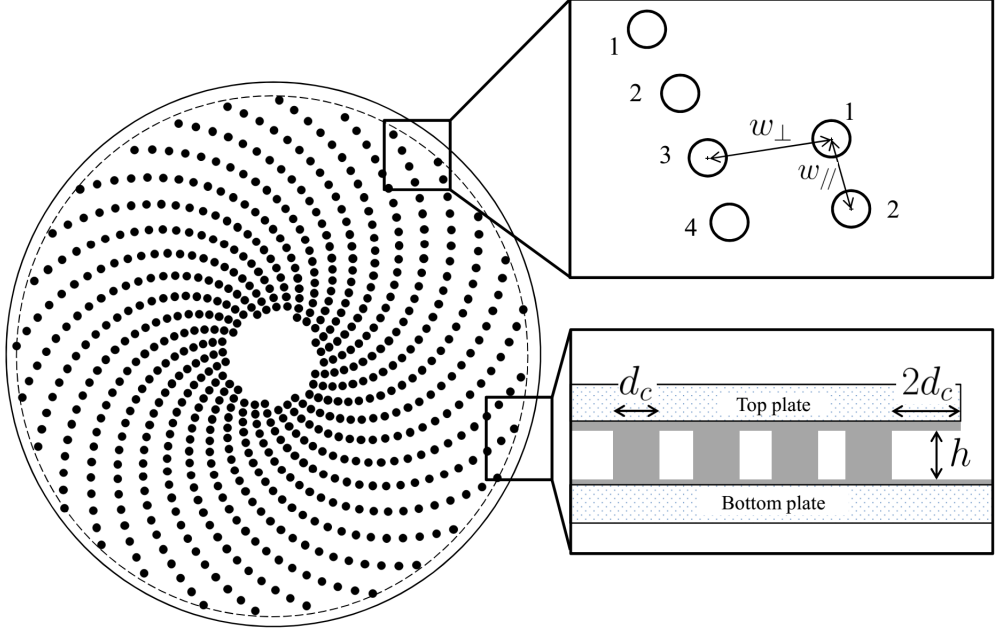


FIGURE 1. Micromodel pattern. Top-right insert: along a given spiral, the center-to-center distance between two cylinders is denoted $w_{//}$ whereas the distance between a cylinder and its closest neighbour in the adjacent spiral (in the counter-clockwise direction) is denoted w_{\perp} . Bottom-right insert: side view of the micromodel edge, for the large micromodel with $d_c = 500 \mu\text{m}$ and $h = 525 \mu\text{m}$. The distance between the circular top plate and the rim of the cylinders pattern is $2d_c$. The SU8 photo-resist appears in gray. Note there is no glass top-plate for the small micromodel ($d_c = h = 50 \mu\text{m}$): the DF1020 top film is directly laminated on the pattern of cylinders.

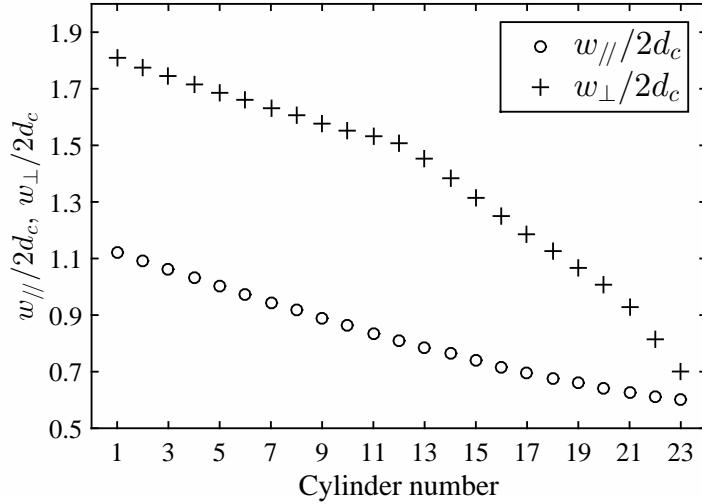


FIGURE 2. Distance between neighbouring cylinders, $w_{//}$ and w_{\perp} (see Figure 1), made dimensionless by dividing by twice the cylinder diameter d_c , plotted as a function of the cylinder number along a given spiral.

Liquid	ρ_f (g cm ⁻³)	μ_f (mPa s)	γ (mN m ⁻¹)	D (mm ² s ⁻¹)	Vapor pressure (kPa)
Hexane	0.657 ± 0.001	0.30 ± 0.003	18.4 ± 0.1	7.65 ± 0.45	17.6 ± 1
Heptane	0.682 ± 0.001	0.40 ± 0.005	19.95 ± 0.1	7.2 ± 0.1	5.2 ± 0.3
Octane	0.7015 ± 0.001	0.53 ± 0.01	21.4 ± 0.1	6.25 ± 0.5	1.55 ± 0.1
Nonane	0.7165 ± 0.001	0.71 ± 0.01	22.7 ± 0.1	5.5 ± 0.5	0.47 ± 0.03
Decane	0.7285 ± 0.001	0.90 ± 0.01	23.65 ± 0.1	5.4 ± 0.25	0.14 ± 0.01

TABLE 1. Working liquid properties at 22°C: ρ_f , μ_f , γ and D correspond to liquid mass density, dynamic viscosity, surface tension and vapor diffusion coefficient in air, respectively.

2.2. Protocol for a drying experiment

The micromodel is positioned horizontally on top of a plane LED light source (Phlox LedW-BL) and is imaged from the top by a sCMOS Lavision camera with a 2048×2048 pixels sensor. The micromodel and LED back-light are therefore perpendicular to the optical axis. The spatial resolution is typically around 1.8 pixel per micron (for micromodels with $h = d_c = 50 \mu\text{m}$). The images are acquired at a fixed acquisition rate, from 0.01 Hz to 100 Hz depending on the experiment. The LED light source is triggered by an external source and synchronized with image acquisition. A small droplet of the working liquid is gently deposited at the edge of the device and then fully fills the micromodel by capillary suction. Image acquisition is then immediately launched to follow the liquid evaporation. The experiments are performed in a temperature-controlled environment, with $T = 22 \pm 1^\circ\text{C}$. Evaporation takes place in a stagnant and “dry” air atmosphere: there is no imposed external air flow and the vapor concentration in the room is assumed to be zero.

Several liquids were used and their relevant thermophysical properties are listed in Table 1. Data for dynamic viscosity μ_f and vapor pressure at the working temperature were obtained using tabulated values and estimating methods proposed by Reid *et al.* (1987). Data for surface tension are from Jasper & Kring (1955). The error bars given come from the uncertainty on the working temperature, $\pm 1^\circ\text{C}$. Data for the vapor-air diffusion coefficient D were obtained from various references (Altshuller & Cohen 1960; Cummings & Ubbelohde 1953; Lugg 1968; Elliott & Watts 1972; Beverley *et al.* 1999) and extrapolated to $22 \pm 1^\circ\text{C}$ using expressions for temperature corrections found in Vargaftik (1975). The uncertainties on D indicated in Table 1 were estimated from the scatter in the available data. All these liquids perfectly wet SU8 and DF1020: when a drop is deposited on a flat SU8 or DF1020 substrate, the liquid fully spreads, rendering any measurement of the contact angle unfeasible. In the following, the contact angle will therefore be assumed to be zero.

2.3. Image processing

In the present study, all the relevant experimental data (i.e. evaporation rates, phase distribution and liquid film extent) were obtained by image processing. A typical image obtained with the CCD camera is shown in Figure 3a. The meniscus surrounding the central liquid cluster deviates the almost parallel light coming from the backlight and appears as the darkest region on such an image. This is better seen on the close-up on the region of interest delimited by the dotted rectangle in Figure 3a, see Figure 3b, where the cylinders embedded in the liquid cluster can also be seen. The very good spatial resolution and the wide dynamic range of such images allow to perform quantitative

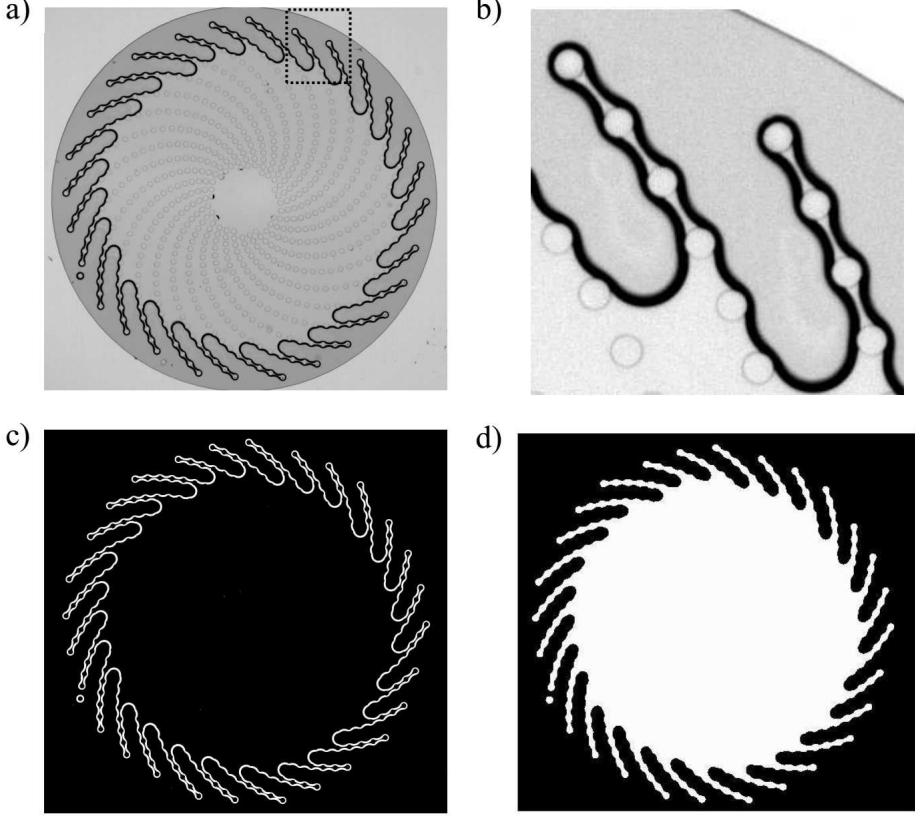


FIGURE 3. Typical image of a micromodel. a) Raw image, for a micromodel filled with heptane, with a resolution of 1.8 pixel per micron; b) Zoom on the region of interest delimited by a dotted rectangle in a); b) Binarized image. c) Binarized image after filling of the central liquid cluster.

measurements at the scale of the cylinders, e.g. regarding the width of the liquid bridges connecting two neighbouring cylinders, along a spiral.

The volume of liquid contained within the micromodel can be measured by image processing, at any time of the drying experiment, as explained in the following. The contrast between the dark meniscus region and the bulk fluid regions (liquid or air) is large enough so that applying a binarization operation is straightforward, leading to the image shown in Figure 3c, which is then filled, Figure 3d. On such an image, the total area of the white region, A , can be readily obtained by image processing (using the Matlab *regionprops* built-in function). Similarly, one can detect any cylinder that is no longer wet by the liquid and thus appears as an isolated disk. Knowing the total number of cylinders, one can have a first estimate of the liquid volume V in the micromodel: $V = A \times h - N_w \times V_p$ where N_w is the measured number of cylinders embedded in the liquid cluster and $V_p = \pi h d_c^2 / 4$ the volume of a cylinder. Then, one has to note that the white region of area A seen in Figure 3c takes into account the projected area of the meniscus. This latter area, A_m , can be obtained from the image shown in Figure 3b, before the filling operation is applied. In the meniscus region, the liquid is not present over the full height h of the micromodel and this has to be taken into account. In fact, the formula above giving V over-estimates the liquid volume, whereas the alternate expression $V = (A - A_m) \times h - N_w \times V_p$ underestimates it.

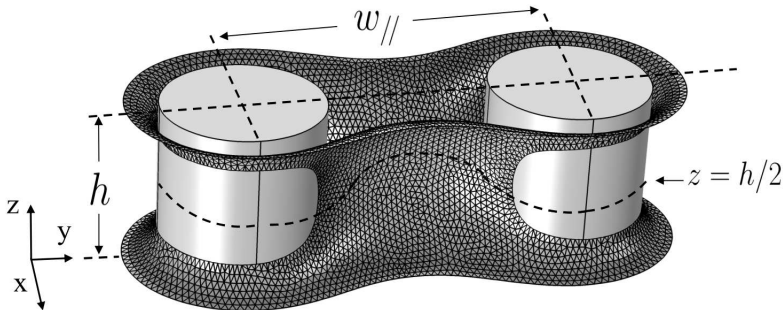


FIGURE 4. a) Typical liquid bridge capillary shape obtained from Surface Evolver. The liquid bridge is trapped between two cylinders and confined between two flat surfaces located in the $z = 0$ and $z = h$ planes (not displayed). The two cylinders, of diameter d_c appear in light gray and are separated by $w_{//}$ (here, $w_{//} = d_c$). The contact angle between the liquid and the solid surfaces is 0° .

To estimate the amount of liquid in the meniscus region, we used the software Surface Evolver (Brakke 1992) to simulate the capillary shape of a static liquid bridge located in between two cylinders, confined in between two horizontal plates. Starting from an initial “guess” shape for the static liquid bridge, Surface Evolver progressively converges towards the meniscus shape minimizing the surface energy, given a set of given constraints (e.g. contact angle on solid surface and liquid volume). During the evolution procedure, the surface can be progressively refined by the user, by increasing the number of facets that shape it. In the present study, shape convergence was typically considered to be reached when the surface energy varied by less than 0.2 % between two successive surface evolution steps, its value being at the same time “robust” to operations like surface refinement, vertices averaging, etc... Let’s consider a typical liquid bridge shape, as shown in Figure 4. We introduce λ such that the liquid content in the meniscus region is $\lambda \times A_p h$, where A_p is the projected meniscus area in the $z = 0$ plane. The coefficient λ can be computed from liquid bridge shapes obtained by Surface Evolver simulations. It depends on the spacing $w_{//}$ between the cylinders, on the liquid volume trapped in the liquid bridge and on the contact angle. The values obtained for λ typically ranges between 0.13 and 0.2. In the following, we assume that the volume of liquid volume V in the micromodel can be obtained as $A \times h - (1 - \lambda)A_m \times h - N_w \times V_p$, where A , A_m and N_w are obtained by image processing as explained above, and taking λ equals to a single typical value of 0.16. This comes down to assume that the liquid content in the meniscus region can be estimated by determining λ on the similar, but simpler, liquid bridge geometry shown in Figure 4.

This image processing-based technique for measuring the liquid content in the micromodel was validated against mass measurements performed with a Mettler-Toledo MS603S balance with a ± 0.001 g accuracy. Such a validation test was performed with the large micromodel only ($h = 525 \mu\text{m}$) for which the mass of liquid is around 0.3 g at the beginning of an experiment whereas it is 3 orders of magnitude smaller, well below the scale minimum weight limit, in the micromodels with $h = 50 \mu\text{m}$ used in the drying experiments. Figure 5 compares the mass-data from the balance (squares symbols) to those obtained by image processing (after multiplying the measured liquid volume by the liquid mass density). Crosses show the data obtained when the amount of liquid in the meniscus region is neglected ($\lambda = 1$) whereas dots show the data corrected taking $\lambda = 0.16$. The latter match nicely the data obtained from the balance. Note that taking

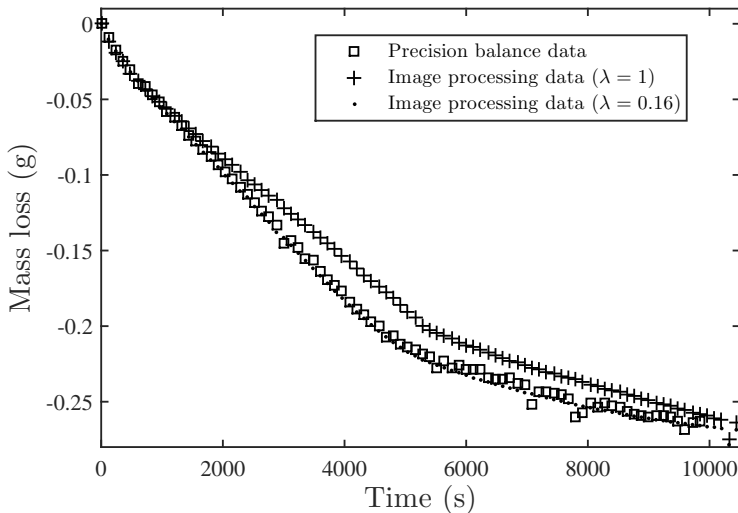


FIGURE 5. Mass loss during evaporation of heptane in a large micromodel ($h = 525 \mu\text{m}$). Squares: data from a precision balance; crosses, respectively dots: data from liquid volume measurements by image processing with $\lambda = 1$ (no liquid in the meniscus region), respectively $\lambda = 0.16$.

$\lambda = 0.13$ or 0.19 results, at most, in a negligible 2.5% variation of the mass obtained by image processing.

3. Experimental results

3.1. Phase distribution and evaporation rate as a function of time

Figure 6 shows the liquid-gas distribution at four successive times, $t = 0$ (beginning of the experiment), $t = 18\text{ s}$, $t = 62\text{ s}$ and $t = 125\text{ s}$, for evaporation of heptane. The experiment starting time, $t = 0$, is taken when the meniscus is fully positioned around the external end of the pattern, see Figure 6a. From $t = 0$ to $t = 18\text{ s}$ approximately, one can observe a progressive invasion of air between the spirals. Concomitantly with the gas phase ingress, some elongated liquid films remain trapped along each spiral. In fact, the distances $w_{//}$ between two cylinders along a spiral are typically small enough to allow for coalescence between the liquid clusters left around each cylinder following air invasion, liquid clusters that would otherwise remain isolated (Chen *et al.* 2017). A liquid film can be described as a chain of liquid bridges between neighbouring cylinders, that first extends up to the spiral most external cylinder, see Figure 6b. At longer times ($t > 18\text{ s}$), the elongated films start to recede in the system. This is caused by successive break-ups of the most external liquid bridge of each elongated film. Thus, an elongated liquid film “depins” progressively from each cylinder of the spiral, while the phase gas ingress continues. This invasion process is described in more details in the next subsection.

The evaporation rate, $E = -dV/dt$, where V is the liquid volume measured by image processing as described earlier, is shown in Figure 7. A quasi-constant evaporation rate period (CRP) is observed with $E_{CRP} \approx 4.5 \times 10^{-3} \mu\text{l s}^{-1}$, from $t = 0$ to $t = 18\text{ s}$. Once the elongated liquid films start to depin from the outermost cylinders, around $t = 18\text{ s}$, a sharp decrease of the evaporation rate is observed. The phenomenology discussed above is observed for all the liquids used. It is similar to the one obtained during the drying of

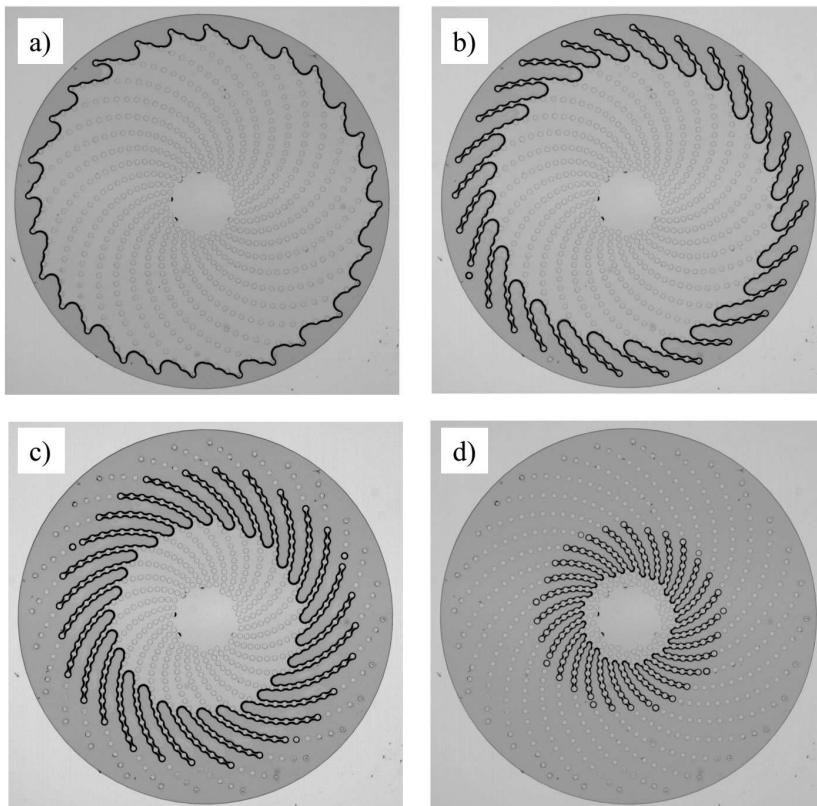


FIGURE 6. Evaporation of heptane in a $50\text{ }\mu\text{m}$ -thick micromodel: phase distribution at $t = 0\text{ s}$ (a), $t = 18\text{ s}$ (b), $t = 62\text{ s}$ (c) and $t = 125\text{ s}$ (d).

capillary porous media and of square cross-section capillary tubes initially filled with a volatile liquid, as discussed in the Introduction.

3.2. Phase distribution evolution at pore scale: an invasion process

To describe the phase distribution at pore scale, we will describe a given liquid film as a chain of connected liquid bridges, positioned between each pair of neighbouring pillars along a spiral. Then, the space between two spirals will be described as a succession of pores, each pore throat being located in between pairs of neighbouring pillars in adjacent spirals. Each liquid film will be marked out using the number of the most external cylinder wet by the liquid and connected to the main, central liquid cluster, i.e. using a number between 1 and 23. Similarly, each main meniscus location within the micromodel will be marked out by the number of the pore it occupies. A sketch detailing these conventions is shown in Figure 8a. Note that such a representation allows to compare readily experiments performed with different liquids, even if the experiments duration changes a lot from one liquid to another, depending on the liquid volatility.

In Figure 8b, the location of the film end (i.e. the location the external tip of the chain of liquid bridges forming the film) is plotted as a function of the main meniscus location for a given “pair” liquid film-main meniscus, in an experiment performed using heptane as evaporating liquid. For each recorded image, these two locations are determined by image processing. Film and main meniscus locations only take integer values between 1 and 23, see open circles in Figure 8b. The data points corresponding to the beginning

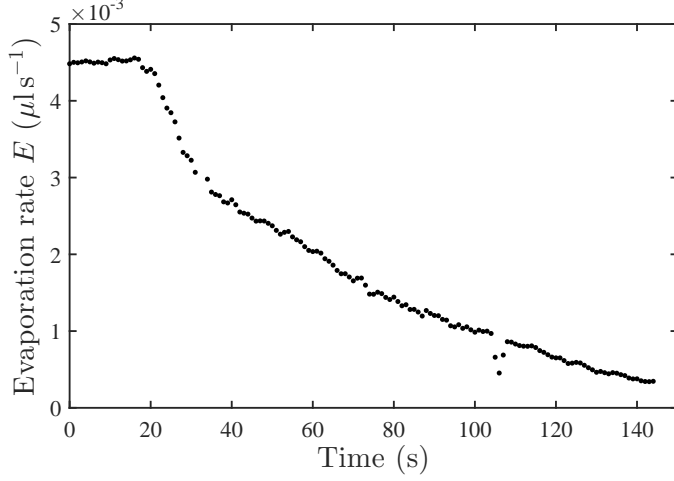


FIGURE 7. Evaporation of heptane in a $50\text{ }\mu\text{m}$ -thick micromodel: evaporation rate E (in μs^{-1}) as a function of time.

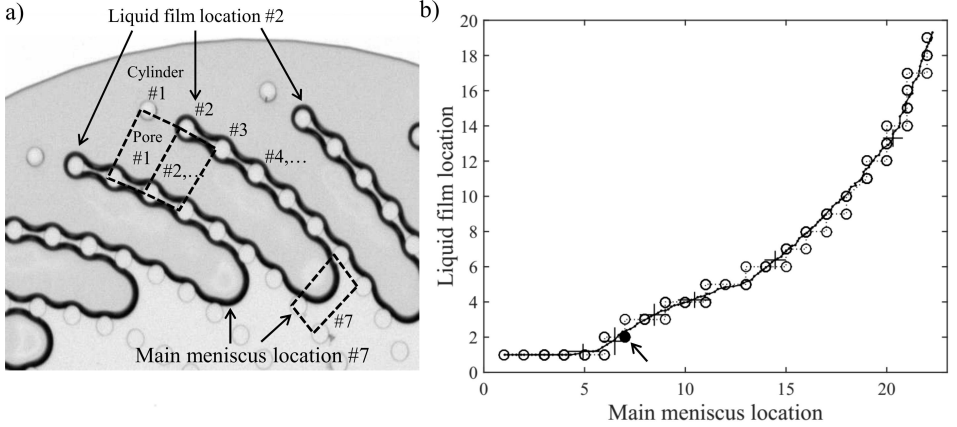


FIGURE 8. a) Sketch showing the way main menisci and liquid films locations are marked out. As an example, for the three spiral ends seen on this close-up of the micromodel, the liquid film location is at cylinder #2. Two main meniscus at location #7 are also highlighted by an arrow. b) Liquid film end location as a function of the main meniscus location, for an drying experiment performed with heptane. Open circles and dotted line: data for a given pair liquid film-main meniscus. The filled black circle highlighted by an arrow marks out the data point corresponding to the particular situation depicted in Figure 8a. Solid line: data averaged over the 28 liquid film-main meniscus pairs of the micromodel. The error bars show the standard deviations to the mean values of liquid film ends and main menisci locations.

of the experiments are in the lower left corner of the graph. As both film end and main meniscus recede towards the micromodel center with time, they are both marked out by larger and larger numbers.

It is important to note that both locations evolve in a discontinuous manner. First, the main meniscus “jumps” from one pore entrance to the next. This motion is a simplified version of the so-called Haines jumps observed in more realistic porous media, (see e.g. Berg *et al.* 2013; Singh *et al.* 2017b). As an example, the displacement of a given main meniscus was extracted from a stack of images taken at a high acquisition rate (100 Hz). Figure 9 shows the meniscus curvilinear coordinate along the dotted white line seen

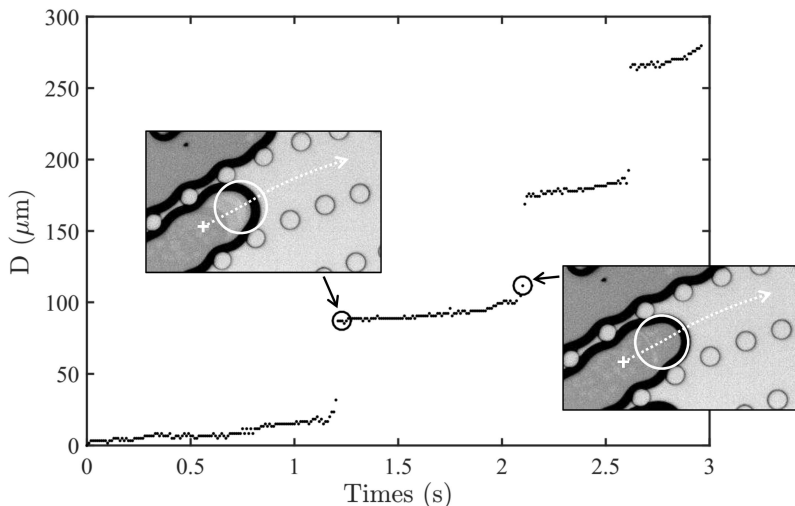


FIGURE 9. Displacement of a given main meniscus as a function of time. The length D is the interface curvilinear coordinate along the white dotted line see on the inserts (the origin $D = 0$ being taken at the cross-marked, left end of the dotted line). The left insert shows the meniscus location just after its jump at the pore entrance it is located. The right insert shows the main meniscus location just before its next jump. On the two inserts, the circle in white is the circle inscribed in between the two pillars that mark the entrance of the pore about to be invaded.

on the two inserts, as a function of time. It is clearly seen that the invasion proceeds by successive jumps: the main meniscus, positioned at the entrance of a given pore, first slowly penetrates into the pore before a sudden jump occurs and drives the main meniscus to its next position, at the entrance of the next pore. In Figure 9, the two inserts display the images taken just after a jump (at $t = 1.23$ s) and just before the next one (at $t = 2.1$ s). Second, the location of the film end is controlled by successive break-ups of the most external liquid bridge of the chain of liquid bridges forming the film. As an example, the width of the most external liquid bridge along a film is plotted as a function of time in Figure 10: it decreases continuously with time until the break-up suddenly occurs, between $t=25$ and $t = 26$ s. Studying in detail the dynamic of the non-local fluid redistribution within the liquid cluster following a pore invasion or of the liquid bridge break-up is not within the scope of the present study. Such topics have been considered in recent studies, using micromodels (Armstrong & Berg 2013) or packing of beads (Singh *et al.* 2017a).

On Figure 8b, the solid line shows the evolution of the liquid films ends as a function of the main menisci locations, averaged over the 28 spirals of the micromodel (so 28 pairs liquid film-main meniscus). A data point is obtained for each recorded image and due to averaging, non-integer values are obtained, the error bars being taken as the standard deviations to the means. The constant evaporation rate period seen in Figure 7 corresponds to the period during which the liquid films are connected to the spiral end, i.e. to cylinder #1. As can be seen in Figure 6b, there are some slight differences from one spiral to another, as far as the main meniscus locations are concerned and also regarding the most external cylinders wet by the liquid. Such slight discrepancies, at a given time, from one pair liquid film-main meniscus to another can be appreciated owing to the errors bars shown in Figure 8b, for a limited set of data points (for sake of clarity). Note that while the errors bars amplitude is roughly constant during a first stage for which the main menisci locations are in the range $[6-12]$, it noticeably decreases as the liquid

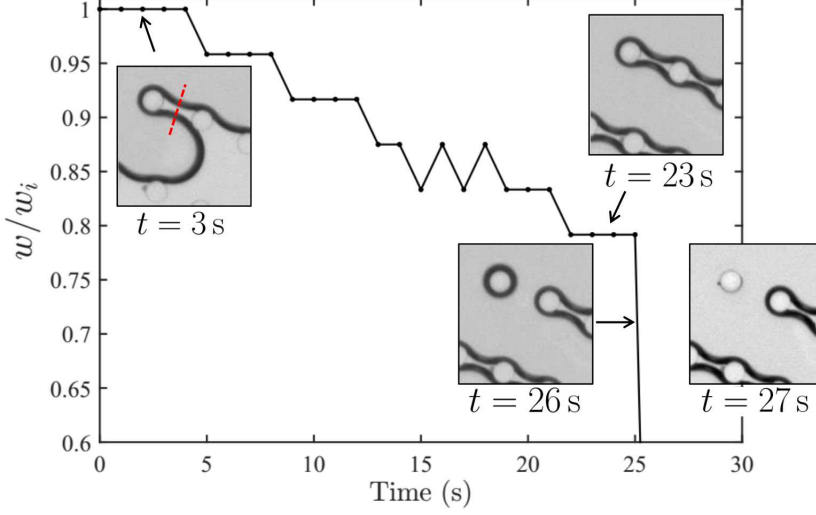


FIGURE 10. Break-up of a liquid bridge (fluid: heptane). The liquid bridge width w , measured along the dotted line shown in the top-left insert, made dimensionless by its initial value w_i , is shown as a function of time. The inserts display the liquid bridge as seen on the images. The break-up occurs between $t=25$ and $t = 26$ s and w/w_i falls to 0. After the break-up, the presence of isolated liquid rings around the external cylinder base and top is demonstrated by the sharp black ring around the cylinder. Such an optical signature of the liquid rings disappears as the liquid contained in the rings evaporates (see image at $t = 27$ s).

cluster becomes more confined in the micromodel center, remark the smaller errors bars for main menisci location beyond 13. Also, it is important to state that such errors bars do not come from the fact that the invasion pattern is slightly out-of phase from one spiral to another but really from small differences in the invasion pattern itself, i.e. on the exact succession of main menisci and film tip locations.

3.3. Experimental results for the different liquids used

In Figure 11, results using averaged values are shown for the various liquids used in the present study. All the curves display the same typical shape. First, the main meniscus recede while the tips of the elongated films remain pinned to the most external cylinder (liquid film location value is then 1). Depinning from the most external cylinder occurs all the more early (in terms of main meniscus location) than the fluid is volatile or, equivalently, than the capillary number is high (see below). The differences between from one liquid to another become less pronounced when the liquid cluster is confined in the center of the micromodel (typically for main meniscus locations larger than #17 and film locations larger than #7). Note that drying experiments were repeated several times (3 to 5 times) for each liquid with a very good reproducibility: one can hardly discern some differences from one experiment to another when their results are plotted on the same graph. Therefore, the slight difference seen in Figure 11 between heptane and hexane is significant: in average, the first liquid bridge break-up occurs earlier with hexane (dots) than with heptane (crosses) and the liquid films observed with hexane are typically one liquid bridge shorter than with heptane, during most of the experiment duration.

Table 2 recapitulates the results obtained for the several liquids used, regarding the evaporation rate measured during the CRP, E_{CRP} , the capillary number Ca (introduced and discussed in §4.2), and the liquid film length evolution during drying. Table 2

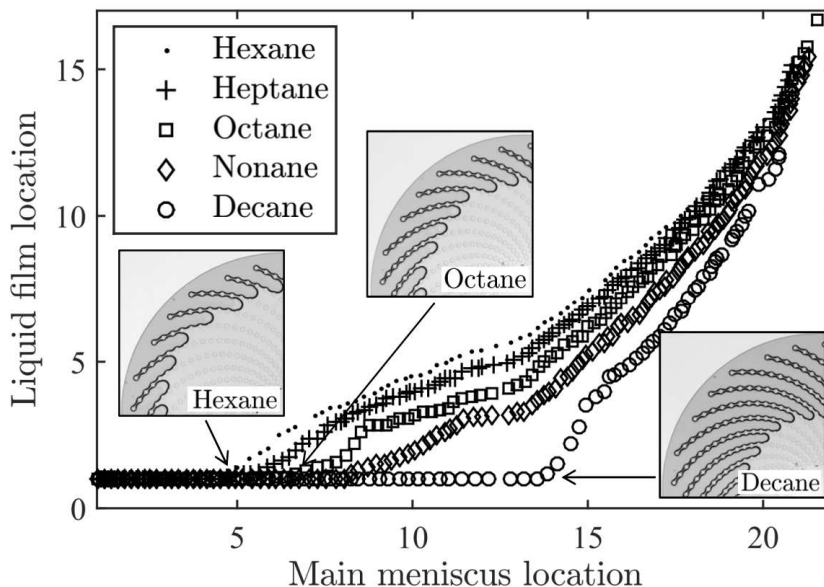


FIGURE 11. Drying experiments: averaged location of the liquid films ends as a function of the averaged location of the main menisci, for the various liquids used (see legend for details). The three inserts display the phase distribution just before depinning, and thus at maximal film extent, for hexane, octane and decane.

	E_{CRP} (μs^{-1})	Capillary number Ca	L_1	L_4
Hexane	$(12.85 \pm 0.5) \times 10^{-3}$	7.3×10^{-5}	5.0 ± 0.5	9.7 ± 0.5
Heptane	$(4.615 \pm 0.1) \times 10^{-3}$	3.18×10^{-5}	5.9 ± 0.5	11 ± 0.7
Octane	$(1.35 \pm 0.02) \times 10^{-3}$	1.16×10^{-5}	7.5 ± 0.6	13 ± 0.25
Nonane	$(4.17 \pm 0.1) \times 10^{-4}$	4.25×10^{-6}	9.8 ± 0.75	14.3 ± 0.5
Decane	$(1.135 \pm 0.05) \times 10^{-4}$	1.57×10^{-6}	14.2 ± 0.4	15.6 ± 0.6

TABLE 2. Experimental results: evaporation rate during the CRP (E_{CRP}), capillary number Ca as defined by equation 4.5 in §4.2, mean main meniscus locations at depinning from the most external cylinder (#1), L_1 , and mean main meniscus locations when the films depin from cylinder # 4, L_4 . The uncertainty is taken as the standard deviation to the mean obtained when averaging data from several experiments, performed with a given liquid.

gives the averaged main meniscus locations when depinning occurs from cylinder #1 and #4, denoted L_1 and L_4 respectively. In the next section, the emphasis will be on the understanding of the liquid films dynamics, i.e. on the prediction of the typical curve shape displayed in Figure 11, including L_1 and L_4 values. The values of E_{CRP} are discussed in Chen *et al.* (2017).

4. Theoretical modelling

We now turn to the theoretical modelling of the micromodel drying. The goal is to be able to predict, for the different liquids used, the phase distribution evolution during drying, i.e. the succession of liquid bridges break-ups and pore invasions. As seen in §3.2, the main meniscus ingress takes the form of jumps from one pore to the next one. Invasion occurs when the capillary pressure, $P_c = P_{gas} - P_{liquid}$, reaches a threshold which is a

function of the geometry of the pore considered: this invasion pressure will be denoted $P_{inv,i}$. As the spatial density of the cylinders increases from the edge to the center of the micromodel, the pores that are successively invaded by the gas are getting narrower and narrower as evaporation proceeds. Therefore, $P_{inv,i}$ increases as i increases. In between two successive pore invasions, when the main meniscus is pinned to a particular pore entrance, the capillary pressure slightly increases as evaporation proceeds, because the meniscus curvature increases until a next Haines jump occurs.

If one assumes that capillary equilibrium is maintained all over the liquid-gas interface during drying, the pressure in a liquid film along a spiral must then also progressively increases. Consequently, each of the liquid bridges that form the liquid film must get thinner and thinner, which is observed experimentally, see Figure 10. Of course, the liquid bridges cannot thin indefinitely and there must exist a critical pressure for which the liquid bridges break-ups. This critical pressure is expected to be all the more small that the spacing between the two pillars of a given liquid bridge is large. That's why break-up occur at the most external liquid bridge of a film. In the following, we will denote $P_{crit,i}$ the critical pressure for the liquid bridge trapped in between cylinders $\#i$ and $\#i+1$.

In a purely capillary scenario, starting from a given main meniscus-liquid film configuration, the invasion process will be controlled by the respective values of $P_{inv,i}$ and $P_{crit,i}$. The invasion scenario is more complex if the viscous pressure drop due to the evaporation-induced flow within the liquid films is such that the liquid-gas interface can no longer be considered as being at capillary equilibrium. In this case, any prediction of the invasion pattern requires the knowledge of the pressure distribution in the liquid, along the film.

In the remaining of the present section, we first obtain estimates of $P_{inv,i}$ and $P_{crit,i}$, before turning to the computation of the viscous pressure drop along the liquid films. Then, theoretical predictions of the invasion pattern, in a purely capillary case and in visco-capillary cases as well, will be compared to the experimental results. Note that the effect of gravity will be neglected in the following. In fact, the Bond number in our experimental setup can be defined as $\rho_l g h^2 / \gamma$. Taking $\gamma \approx 20 \times 10^{-3} \text{ N m}^{-1}$ and $\rho_l \approx 0.8 \text{ g cm}^{-3}$ for the liquids used (see Table 1), one obtain $Bo \approx O(10^{-3})$ with $h = 50 \mu\text{m}$. Also, the present modelling is isothermal: we neglect any cooling effect induced by evaporation (which would change the physical properties of the liquid, depending on its position relative to the evaporative front). Such an assumption was made by Chauvet *et al.* in their study of evaporation in square cross-section capillary tubes. Measurements of the external tube wall temperature by infra-red thermography revealed a maximal cooling localized at the tube top, opened end not exceeding a few degrees Celsius for hexane, the most volatile liquid used (Chauvet 2009; Chauvet *et al.* 2010a). An isothermal modelling was shown to be in good agreement with the experimental measurement performed (maximal corner film length notably), see Chauvet *et al.* (2010b). The evaporation rate measured in the present study are of the same order of magnitude, $O(10^{-9} \text{ kg s}^{-1})$, as those reported by Chauvet *et al.* and the characteristic size of the micromodel, $O(\text{mm})$, is similar to that of the tip of the capillary tubes used by Chauvet *et al.*. Also, the micromodel glass bottom plate has a high-thermal conductivity. For these reasons, we expect the isothermal assumption to be correct in the present geometry.

4.1. Critical capillary pressure of a liquid bridge and pore invasion pressure

A key point of the above scenario is that there is a critical capillary pressure (or equivalently critical curvature) above which a liquid bridge cannot be sustained in between two neighbouring cylinders. This point was studied using the software Surface

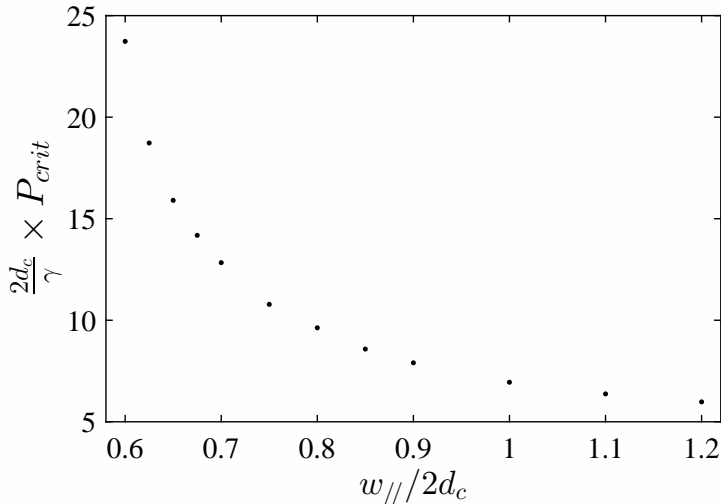


FIGURE 12. Critical capillary pressure for liquid bridge break-up. The capillary pressure $P_{gas} - P_{liquid}$ is made dimensionless by dividing by $\gamma/2d_c$ and is plotted as a function of the dimensionless center-to-center distance between the two cylinders, $w_{//}/2d_c$. The contact angle of the liquid on the cylinders and on the top and bottom plates is zero.

Evolver (SE), by simulating the shape of single liquid bridges trapped between two cylinders, confined in between two horizontal plates. Such liquid bridges can be considered as the building block of the elongated liquid films that are observed along each spiral in the experiment. Typically, for a given spacing between the two cylinders, a converged liquid bridge shape was computed as a function of the liquid volume. The equilibrium capillary pressure and relevant geometrical parameters describing the liquid bridge were obtained for each volume step. We assume that the liquid bridge breaks-up occurs when its thickness t at the location $(x = 0, y = w_{//}/2, z = h/2)$, see Figure 4, tends toward zero (simulations are typically stopped when $t/2d_c = 0.01$). The critical pressure for a liquid bridge is then the one obtained in SE “just before” the two liquid-gas interfaces collapses. Figure 12 shows the evolution of the dimensionless critical pressure, $2d_c \times P_{crit}/\gamma$ obtained in SE for a zero contact angle, as a function of the dimensionless spacing between the two cylinders $w_{//}/2d_c$. As expected, the critical pressure increases when $w_{//}$ decreases. Results for different contact angles and details in the use of SE are given in Chen (2016).

In the experiment, the elongated liquid films observed consist of chains of connected liquid bridges and break-up occurs systematically for the most external liquid bridge. To check if the critical capillary pressure obtained for an isolated liquid bridge is a fair approximation of the critical pressure at play in the experiment, some SE simulations were also ran along a chain of cylinders with varying distances between the cylinders, corresponding to those imposed by the microfabrication design. Capillary shapes of elongated films were obtained for successive, decreasing liquid volumes until the liquid bridge break-up occurs in between the two most distant cylinders. The critical pressure found when considering a chain of N cylinders (i.e. $N - 1$ liquid bridges), made dimensionless by its value for $N = 2$, was found to vary by less than 1 %, whatever N is, compared to the reference case ($N = 2$).

Another key element of the basic invasion mechanism exposed above is the knowledge of the capillary pressure to be reached to invade a given pore, $P_{inv,i}$. As seen in Figure 10, the liquid-gas interface just before invasion of pore $\#i$ closely matches the circle inscribed

in between the two pillars highlighted in red, i.e. the opening of the pore about to be invaded. Such an observation was repeated over several invasion events. Consequently, the invasion capillary pressure for a given pore $\#i$ is estimated as:

$$P_{inv,i} = \gamma \left(\frac{2}{D_i} + \frac{2}{h} \right), \quad (4.1)$$

where $2/D_i$ is the curvature of the interface in the observation plane with $D_i = w_{\perp,i} - d_c$, h is the micromodel thickness and the liquid is perfectly wetting (zero contact angle). Note that D_i is a function of the pore considered and decreases as one penetrates further into the micromodel.

4.2. Viscous pressure drop within the liquid films

To estimate the viscous pressure drop due to the evaporation-induced flow within the liquid films, we again regard the liquid film as a succession of connected liquid bridges. A pressure drop $\Delta P_{\mu,i}$ is defined for each liquid bridge i (located between cylinders i and $i + 1$) as the flow-induced pressure difference between the liquid bridge inlet and outlet, located in plane $y = 0$ and $y = w_i$ respectively, see Figure 4. The invasion algorithm in a visco-capillary case, described in the next subsection, will require an estimate of the pressure in the middle of each liquid bridge i , for a given position j of the main meniscus:

$$P_{lb,i} = P_{inv,j} - \left(\frac{\Delta P_{\mu,i}}{2} + \sum_{k=i+1}^{k=j-1} \Delta P_{\mu,k} \right). \quad (4.2)$$

To calculate $\Delta P_{\mu,i}$, we follow the classical analysis of Ransohoff & Radke (1988) for corner flows, that relates the pressure drop to the flow rate in the liquid film by a Poiseuille-like law:

$$\Delta P_{\mu,i} = \frac{\beta}{R_{in,i}^2} \mu_f w_{//,i} \frac{q_i}{A_{in,i}}. \quad (4.3)$$

In this expression, q_i is the liquid flow rate in the liquid bridge, $A_{in,i}$ the liquid bridge total cross-section area in the $y = 0$ plane and β a dimensionless flow resistance, which is a function of the liquid bridge shape, the contact angle, and of the boundary condition at the liquid-air interface. In the $y = 0$ plane, the liquid bridge consists of four identical liquid corners/wedges, confined between the horizontal plates and the cylinder wall, with a radius of curvature $R_{in,i}$ in the plane $y = 0$.

Use of equation 4.3 requires the knowledge of the liquid bridge shape (A_{in} and R_{in}), of the viscous resistance β , and of the liquid flow rate within the liquid bridge. An extensive set of Surface Evolver simulations of liquid bridges was first performed, giving A_{in} and R_{in} as a function of the capillary pressure and $w_{//}$. The viscous resistance β was then obtained from direct numerical simulations (DNS) of the flow within the simulated liquid bridges (the detailed procedure and validation tests are presented in Appendix I).

Therefore, in the present modelling, the viscous flow-induced pressure drop within each liquid bridge is computed using a liquid bridge shape obtained at capillary equilibrium (i.e. with no flow). As the capillary number is small in the present experiments, deviations from the capillary shape should be small and the present *local equilibrium* assumption is expected to be relevant. Note that avoiding such an assumption would require to simulate the flow within the film together with the film shape, using a volume of fluids (VOF) or a level-set method, for instance. However, such numerical techniques remain numerically challenging and computationally demanding in the case of low capillary number flows, e.g. due to spurious effects such as parasitic currents (Horgue *et al.* 2012; Raeini *et al.*

2012). Use of DNS techniques allowing interface tracking in the present film flow problem is then well beyond the scope of the present paper.

As far as the flow rate within the liquid bridge is concerned, we assume that the pore space remains saturated with vapor during the micromodel drying, due to confinement effects. Such an assumption has been validated by simulations of the stationary vapor concentration field in the pore space, see Chen (2016). As a result, evaporation occurs at the tip of the liquid films only, i.e. around the last cylinder connected to the liquid film and the flow rate q is constant along a liquid film. We also assume that the evaporation rate is evenly distributed around the 28 spirals of the system so that $q = E/28$. The evaporation rate E is measured experimentally, as explained earlier, and its evolution during a drying experiment can be formulated as a function of the location of the liquid films tips: $E = E_{CRP} \times f_i$ where i is the films tips location (i.e. the number of the most external cylinder wet by the liquid films, averaged over the 28 liquid films). The function f_i is such that $f_1 = 1$ and can be obtained experimentally. It is well-fitted by an order 5 polynomials and does not depend on the liquid used.

Finally, equation 4.3 can be manipulated to introduce the relevant, dimensionless capillary number. To that end, we introduce R_0 , a typical order of magnitude for R_{in} , such that $R_{in}/R_0 \approx O(1)$ for all the liquid bridge geometries relevant in the present study. Then,

$$\frac{\Delta P_\mu}{\gamma} = \frac{\mu}{\gamma} \frac{\beta E_{CRP} f_{w//}}{28 \times A_{in} \times R_{in}^2} = \frac{\mu}{\gamma} \frac{E_{CRP}}{28 \times R_0^2} \times \frac{\beta f_{w//} R_0^2}{A_{in} R_{in}^2} = Ca \beta \frac{f_{w//} R_0^2}{A_{in} R_{in}^2} \quad (4.4)$$

where the capillary number Ca is defined as:

$$Ca = \frac{\mu}{\gamma} \frac{E_{CRP}}{28 R_0^2}. \quad (4.5)$$

and can be calculated taking $R_0 = 10 \mu\text{m}$, see Table 2. Note that a Reynolds number for the liquid flow within the liquid films can be defined as $Re = \rho_f u R_0 / \mu_f$, with $u \approx E_{CRP} / (28 R_0^2)$. Such a Reynolds number is in the range $O(10^{-3}) - O(0.1)$ in the experiments.

4.3. Invasion algorithms and comparison between theoretical predictions and experimental results

Once P_{inv} and P_{crit} are estimated, the expected invasion pattern in the capillary case, $Ca = 0$, is obtained straightforwardly. For given locations (i, j) of the liquid films tip and main meniscus respectively (initialization is at $i = 1, j = 2$), one compare $P_{inv,j}$ and $P_{crit,i}$. If $P_{inv,j} < P_{crit,i}$, $j \rightarrow j + 1$, otherwise break-up occurs and $i \rightarrow i + 1$. When the capillary number is non zero, one first needs to compute the liquid pressure distribution along the liquid film. Then, the pressure in the middle of the most external liquid bridge is compared to P_{crit} . More precisely, the visco-capillary algorithm is the following:

(i) The pressure at the liquid bridge $j - 1$, $P_{lb,j-1}$, is initialized at $P_{inv,j}$. The radius of curvature $R_{in,j-1}$ is obtained by extrapolating from the set of Surface Evolver simulations data giving $R_{in,j-1}$ as a function of $P_{lb,j-1}$. The dimensionless evaporation rate is set to $f_{\#j}$. The pressure drop $\Delta P_{\mu,j-1}$ is then computed using equation 4.3.

(ii) The pressure at the liquid bridge is then set to $P_{inv,j} - \Delta P_{\mu,j-1}/2$. This new pressure involves a new liquid bridge shape and so an updated radius of curvature $R_{in,j-1}$ is obtained to compute a new $\Delta P_{\mu,j-1}$. A few iterations are needed for this procedure to converge to stable values for $\Delta P_{\mu,j-1}$ and $P_{lb,j-1}$. Then, liquid bridge $j - 2$ is considered: $P_{lb,j-2}$ is initialized at $P_{inv,j} - \Delta P_{\mu,j-1}$ and the above procedure is repeated until convergence for $\Delta P_{\mu,j-2}$ and $P_{lb,j-2}$.

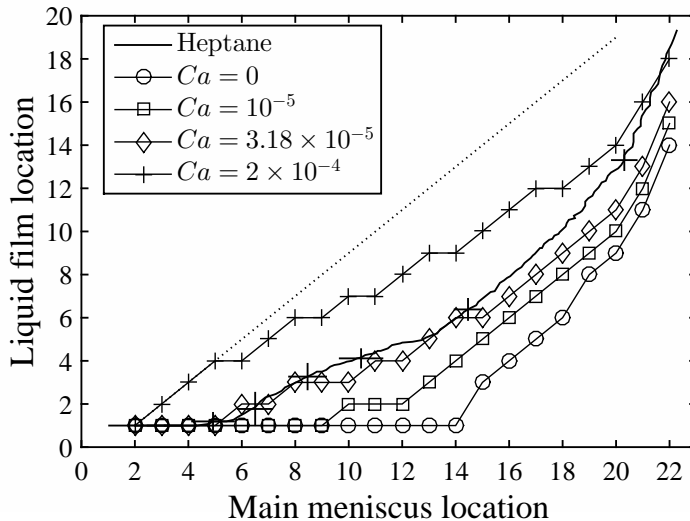


FIGURE 13. Theoretical predictions regarding the liquid film end location as a function of the main meniscus location for 4 different capillary numbers (see legends for details). The solid line is the result obtained for drying experiment performed with heptane at $Ca = 3.18 \times 10^{-5}$, see Table 2 and Figure 8b. The straight dotted line shows the result obtained from the invasion algorithm when no films can develop, i.e. for “large” capillary numbers.

(iii) Once the pressure drops have been obtained for all the liquid bridges, the pressure $P_{lb,i}$ computed from equation 4.2 is compared to $P_{crit,i}$. If smaller, the main meniscus recedes, $j \rightarrow j + 1$. Otherwise, break-up occurs. In this case, the film length is set to be one liquid bridge shorter, $i \rightarrow i + 1$. In both cases, the full algorithm is repeated from step 1 above, to identify the next step of the invasion process (pore invasion or liquid bridge break-up), and so on.

The prediction of the capillary model ($Ca = 0$) are shown as open circles in Figure 13 together with results obtained taking into account viscous effects, for $Ca = 10^{-5}$, 3.18×10^{-5} and 2×10^{-4} , shown as squares, diamonds and crosses respectively in Figure 13. For sufficiently “large” capillary numbers, typically $Ca > 10^{-6}$, deviations from the capillary curve are found. The trend observed as capillary numbers increase is the same as in the experiments, see Figure 11. When the capillary number is large, $Ca > 3 \times 10^{-4}$, no films are formed during the early invasion process. From initialization at $i = 1$ and $j = 2$, the system directly jumps to $i = 2$ and $j = 3$ as the single liquid bridge between cylinder #1 and #2 cannot be sustained. However, the evolution does not follow the dotted line shown in Figure 13 which shows the result obtained from the invasion algorithm when elongated films never develop. When the evaporation rate has sufficiently decreased, the viscous effects decrease and elongated films consisting of several connected liquid bridges can be found (as soon as the main meniscus has receded to location #6 for the $Ca = 2 \times 10^{-4}$ case shown in Figure 13). Note, however, that such a case was not observed in the present experiments. It could probably be observed for highly volatile liquids, for which the present isothermal modelling may be inappropriate.

A qualitative agreement between experiment and theory is shown in Figure 13 for the particular case of drying with heptane, for which $Ca = 3.18 \times 10^{-5}$. This remains true when considering the other liquids used in the present study (data not shown in Figure 13 for sake of clarity) and this can be appreciated in Figure 14, where the main meniscus locations when depinning occurs from cylinder #1 and #4, denoted

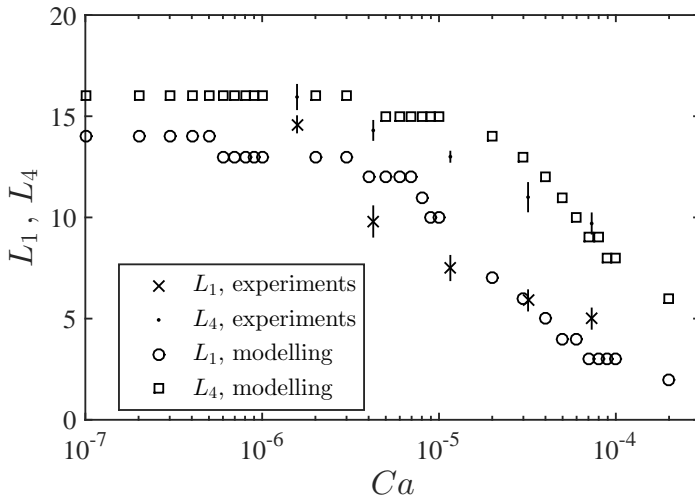


FIGURE 14. Film length, expressed in number of connected liquid bridges, as a function of the capillary number Ca when depinning from cylinder # 1 and # 4 occurs, L_1 and L_4 . Circles, respectively squares: theoretical prediction for depinning from cylinder # 1, respectively #4. Crosses, respectively dots: experimental results for L_1 and L_4 , see Table 2.

L_1 and L_4 respectively, are plotted as a function of the capillary number Ca . The theoretical prediction (squares and circles) converges to the purely capillary case as soon as $Ca < 8 \times 10^{-7}$. The transition to a visco-capillary regime occurs in the range $Ca = 10^{-6} - 10^{-4}$ and is quite sharp. For $Ca > 10^{-4}$, the first liquid bridge cannot be sustained, as discussed above. Experimental data from Table 2 are shown as crosses (L_1) and dots (L_4). Despite some discrepancies, the trend from the theoretical prediction is reproduced and the agreement modelling-experiment is quite satisfactory, given the various approximations made in the modelling, notably the local capillary equilibrium assumption.

5. Conclusion

The main goal of the present study was to investigate the drying dynamics in a model system displaying liquid films with a complex shape. The spatial pattern of the cylinders used in the present study allows to obtain funicular liquid films, i.e. liquid films connecting several cylinders, that can span a large region of the micromodel during the drying process. These liquid films are topologically more complex than the elongated films found in polygonal cross-section capillary tubes. However, their impact on the drying kinetics is the same: by providing a hydraulic connectivity between the central liquid cluster and the micromodel periphery, they are responsible for the constant evaporation rate period. Predicting the maximal extent of the films along the spirals is therefore a key point, which requires the modelling of the liquid transport within the films.

The modelling is based on the straightforward idea of decomposing the films into elementary units, here liquid bridges connecting two neighbouring cylinders. At this local scale, and assuming a local capillary equilibrium, i.e. provided that capillary numbers are small, bridge shape and liquid flow with the capillary bridge can be studied numerically, providing data essential for writing down an invasion algorithm (critical pressure for liquid bridge break-up, pore invasion pressure and resistance to flow within a liquid

bridge). Such a modelling is found to be in qualitative agreement with the experiments, as far as the drying dynamics, i.e. the invasion pattern and extent of films, is concerned. An important effect taken into account is the fact that the viscous effects modify the pressure distribution along the films, leading to a decrease of the films length compared to a purely capillary case. Thus, the present study provides a conceptual framework to deal with visco-capillary drying regimes, at low capillary numbers.

With the general idea of fully understanding/quantifying the liquid films impact on porous media drying, an obvious next step would be to turn to 3D liquid films clusters found in packing of beads. In such clusters, the films have also been shown to be classified in several units (dimer, trimer, etc...), see Scheel *et al.* (2008*a,b*). Also, Cejas *et al.* (2016) recently reported some experiment on the drying of a single column of spherical beads, in a capillaro-gravity regime. Using Surface Evolver simulations, they related the experimentally observed drying kinetics to the topology of the films network, which displays a transition between a funicular and a pendular regime (without long range connectivity) depending on the beads arrangement. However, the extension of a “direct” approach, such as the one used in the present study, to real 3D films network remains elusive due to the complex connectivity of such networks. A more fruitful approach may lie in a fine topological analysis of such films network, in order to localize the regions that control the viscous dissipation and then the pressure evolution within the film (in a viscous regime).

Finally, let’s note that if the knowledge gained by the present study has applications in drying and other porous-media problems involving transport within liquid films, it also may have an interest for microfluidic applications, where control of evaporation is a major issue (see e.g. Clément & Leng 2004). The present study show that such a control may be achieved by finely tuning the microsystem design in order to favor, or not, the transport of a liquid by films (see Chen *et al.* 2017).

6. Appendix DNS of Stokes flow within liquid films

In this appendix, we detail the numerical techniques used to compute the flow within a liquid bridge and obtain the viscous resistance β defined in §4.2. The liquid is supposed to be isothermal, incompressible and Newtonian. Gravity is neglected and the flow Reynolds number is smaller than 1, see §4.2. Therefore, the equations of motion reduce to Stokes equations.

The full numerical procedure, from Surface Evolver (SE) simulations to get the liquid-vapor interface shape to DNS of the Stokes flow, was first validated by computing β for the flow in a right-angle, straight wedge, a case first studied by Ransohoff & Radke (1988). The interface shape is computed using SE for different contact angles between the liquid and the (y-z) and (x-y) planes, see a typical example in Figure 15a. The interface shape obtained from SE is saved as an IGES file that is imported into the finite-element-based commercial software Comsol Multiphysics. Comsol uses free tetrahedral elements to mesh a liquid domain of length L along the y-axis and delimited by the interface and the (y-z) and (x-y) planes. A no-slip boundary condition is implemented on the two contact planes between the liquid and the wedge. Two different boundary conditions can be used at the liquid-gas interface, namely a no-stress boundary condition or a no-slip boundary condition. Finally, a pressure difference ΔP is imposed between the inlet and the outlet planes, separated by a distance L along the y-axis, see Figure 15a. The Stokes

flow is then solved numerically and the dimensionless viscous resistance is obtained as :

$$\beta = \frac{-R_{in}^2}{\mu_f \langle \mathbf{u} \rangle} \times \frac{\Delta P}{L} \quad (6.1)$$

where $\langle \mathbf{u} \rangle$ is obtained by dividing the total liquid flow rate computed by Comsol by the liquid film cross-section area and R_{in} is the interface radius of curvature in the x-z plane (see Figure 15a). Numerical results for β converge as soon as the mesh surface density used in the SE simulations is large enough. Simulations were ran for different contact angle between the liquid and the wedge walls, considering either the no-slip or no-stress boundary conditions. For all the cases investigated, the results of Ransohoff & Radke (1988) regarding β are recovered within less than 1 %.

We now turn to the case of liquid bridges. A typical converged liquid bridge shape has been shown in Figure 4. The unit-cell used for the DNS consists of the liquid bridge part that is in the half-space $x > 0$, confined between the $y = 0$ and $y = w_{//}$ planes on one hand and between the $z = 0$ and $z = h/2$ planes on the other hand, leading to the computational domain shown in Figure 15b. A no-slip boundary condition is implemented on the liquid-cylinders and liquid-bottom plate interfaces, together with the symmetry at the plane $z = h/2$. Similarly to the straight-wedge case, a pressure difference is imposed between the inlet and outlet liquid bridge cross-sections. Computations are ran considering a no-stress boundary condition on liquid-vapor interface. The viscous resistance to the flow is obtained using equation 6.1 where the pressure gradient driving the flow is now defined as $\Delta P_l/w_{//}$. In equation 6.1, R_{in} is now the interface radius of curvature in the (x-z) plane, at the inlet of the computational domain, see Figure 15b. It is determined by fitting the interface profile with a circle. The velocity $\langle \mathbf{u} \rangle$ is computed in the inlet plane. Numerical results for β converge for a SE surface mesh density larger than that found to be necessary for convergence in the straight-wedge case. Also, they were found to be slightly sensitive to the volume-mesh refinement scheme used in Comsol. Finally, we estimate the uncertainty on the values of β obtained to be in the order of 2-3 %.

Figure 15c displays a typical result regarding the pressure field in the liquid bridge. As can be seen, pressure gradients are concentrated close to the liquid bridge inlet and outlet, i.e. in the corner film confined between the cylinder and the flat bottom plane. The pressure gradient is significantly weaker in the central region of the liquid bridge. Figure 16 shows the evolution of β , as a function of $R_{in}/w_{//}$, for various spacing $w_{//}$ between the cylinders and a fixed contact angle ($\theta = 0^\circ$). The trend depicted in Figure 16 is consistent with the liquid bridge shape variation with its volume. A liquid bridge is more “tortuous” for smaller liquid volumes, which is consistent with the increase of the flow resistance with decreasing R_{in} , as smaller volumes mean smaller R_{in} values. More results for β , notably for various liquid-solid contact angles, are given in Chen (2016).

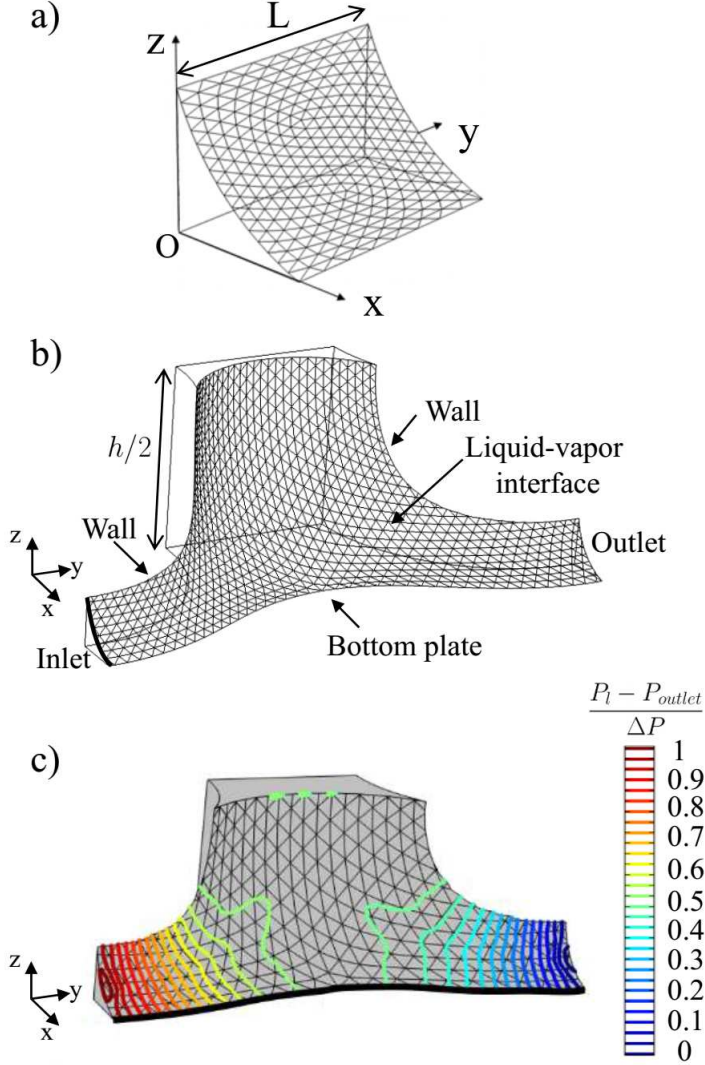


FIGURE 15. a) Typical liquid-gas interface in a right angle, straight wedge computed using Surface Evolver. Here the contact angle θ is 10° ; b) DNS computational domain obtained from a typical liquid bridge shape (see Figure 4); c) Typical computed pressure field in a liquid bridge from Comsol, with a no-stress boundary condition on the interface. Isobars on the liquid-gas interface are shown as colored lines.

REFERENCES

- ALTSHULLER, A.P. & COHEN, I.R. 1960 Application of diffusion cells to production of known concentration of gaseous hydrocarbons. *Analytical Chemistry* **32** (7), 802–810.
- ARMSTRONG, R. T. & BERG, S. 2013 Interfacial velocities and capillary pressure gradients during haines jumps. *Physical Review E* **88** (4), 043010.
- BERG, S., OTT, H., KLAPP, S. A., SCHWING, A., NEITELER, R., BRUSSEE, N., MAKURAT, A., LEU, L., ENZMANN, F., SCHWARZ, J. O. & OTHERS 2013 Real-time 3d imaging of haines jumps in porous media flow. *Proceedings of the National Academy of Sciences* **110** (10), 3755–3759.
- BEVERLEY, K. J., CLINT, J.H. & FLETCHER, P.D.I. 1999 Evaporation rates of pure liquids

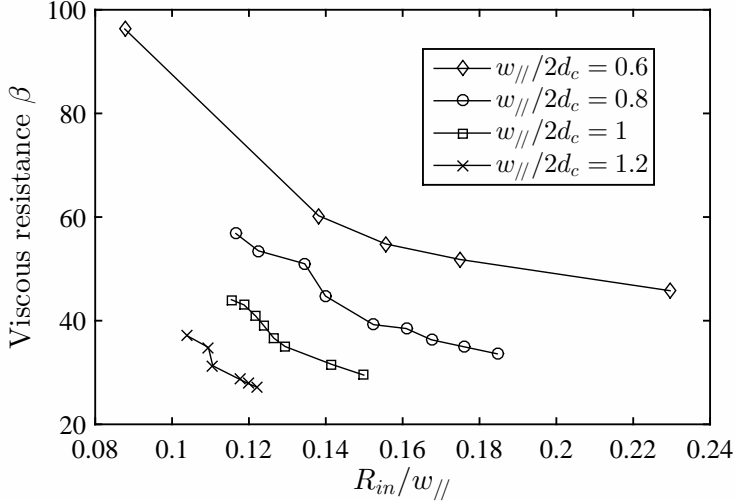


FIGURE 16. Liquid bridge flow resistance β as a function of $R_{in}/w_{||}$ for 4 different spacings between the two cylinders, see legend for details. These numerical results were obtained with a no-viscous-stress boundary condition at the liquid-gas interface and for a 0° contact angle.

measured using a gravimetric technique. *Physical Chemistry Chemical Physics* **1** (1), 149–153.

BRÄKKE, K. A. 1992 The surface evolver. *Experimental Mathematics* **1** (2), 141–165.

CEAGLSKE, N.H. & HOUGEN, O.A. 1937 Drying granular solids. *Industrial & Engineering Chemistry* **29** (7), 805–813.

CEJAS, C. M., HOUGH, L. A., FRÉTIGNY, C. & DREYFUS, R. 2016 Effect of granular packing geometry on evaporation. *arXiv preprint arXiv:1601.04584*.

CHAUVET, F. 2009 Effet des films liquides en évaporation. PhD thesis, Institut National Polytechnique de Toulouse.

CHAUVET, F., CAZIN, S., DURU, P. & PRAT, M. 2010a Use of infrared thermography for the study of evaporation in a square capillary tube. *International Journal of Heat and Mass Transfer* **53** (9), 1808–1818.

CHAUVET, F., DURU, P., GEOFFROY, S. & PRAT, M. 2009 Three periods of drying of a single square capillary tube. *Physical Review Letters* **103** (12), 124502.

CHAUVET, F., DURU, P. & PRAT, M. 2010b Depinning of evaporating liquid films in square capillary tubes: Influence of corners roundedness. *Physics of Fluids* **22** (11), 112113.

CHEN, C. 2016 Evaporation au sein de systèmes microfluidiques: des structures capillaires à gradient d'ouverture aux spirales phyllotaxiques. PhD thesis, Institut National Polytechnique de Toulouse.

CHEN, C., P., DURU, P., JOSEPH, S., GEOFFROY & M., PRAT 2017 Control of evaporation by geometry in capillary structures: from confined pillar arrays in a gap radial gradient to phyllotaxy inspired geometry. *submitted to Scientific Reports*.

CLÉMENT, F. & LENG, J. 2004 Evaporation of liquids and solutions in confined geometry. *Langmuir* **20** (16), 6538–6541.

COUSSOT, P. 2000 Scaling approach of the convective drying of a porous medium. *The European Physical Journal B-Condensed Matter and Complex Systems* **15** (3), 557–566.

CUMMINGS, G.A. McD. & UBBELOHDE, A.R. 1953 Collision diameters of flexible hydrocarbon molecules in the vapour phase: the “hydrogen effect”. *Journal of the Chemical Society (Resumed)* pp. 3751–3755.

DOUADY, S. & COUDER, Y. 1992 Phyllotaxis as a physical self-organized growth process. *Physical Review Letters* **68** (13), 2098.

ELLIOTT, R. W. & WATTS, H. 1972 Diffusion of some hydrocarbons in air: a regularity in

- the diffusion coefficients of a homologous series. *Canadian Journal of Chemistry* **50** (1), 31–34.
- HORGUE, P., AUGIER, F., QUINTARD, M. & PRAT, M. 2012 A suitable parametrization to simulate slug flows with the volume-of-fluid method. *Comptes Rendus Mécanique* **340** (6), 411–419.
- HU, R., WAN, J., KIM, Y. & TOKUNAGA, T. K. 2017 Wettability impact on supercritical co₂ capillary trapping: Pore-scale visualization and quantification. *Water Resources Research* **53** (8), 6377–6394.
- JASPER, J. J. & KRING, E. V. 1955 The isobaric surface tensions and thermodynamic properties of the surfaces of a series of n-alkanes, c₅ to c₁₈, 1-alkenes, c₆ to c₁₆, and of n-decylcyclopentane, n-decylcyclohexane and n-decylbenzene. *The Journal of Physical Chemistry* **59** (10), 1019–1021.
- JUNG, M., BRINKMANN, M., SEEMANN, R., HILLER, T., DE LA LAMA, M. S. & HERMINGHAUS, S. 2016 Wettability controls slow immiscible displacement through local interfacial instabilities. *Physical Review Fluids* **1** (7), 074202.
- KEITA, E., KOEHLER, S. A., FAURE, P., WEITZ, D. A. & COUSSOT, P. 2016 Drying kinetics driven by the shape of the air/water interface in a capillary channel. *The European Physical Journal E* **39** (2), 1–10.
- KOHOUT, M., GROF, Z. & ŠTĚPÁNEK, F. 2006 Pore-scale modelling and tomographic visualisation of drying in granular media. *Journal of Colloid and Interface Science* **299** (1), 342–351.
- LACEY, M., HOLLIS, C., OOSTROM, M. & SHOKRI, N. 2017 Effects of pore and grain size on water and polymer flooding in micromodels. *Energy & Fuels* .
- LAURINDO, J. B. & PRAT, M. 1998 Numerical and experimental network study of evaporation in capillary porous media. drying rates. *Chemical engineering science* **53** (12), 2257–2269.
- LEHMANN, P., ASSOULINE, S. & OR, D. 2008 Characteristic lengths affecting evaporative drying of porous media. *Physical Review E* **77** (5), 056309.
- LENORMAND, R., TOUBOUL, E. & ZARCONI, C. 1988 Numerical models and experiments on immiscible displacements in porous media. *Journal of fluid mechanics* **189**, 165–187.
- LEWIS, W. K. 1921 The rate of drying of solid materials. *Industrial & Engineering Chemistry* **13** (5), 427–432.
- LUGG, G. A. 1968 Diffusion coefficients of some organic and other vapors in air. *Analytical Chemistry* **40** (7), 1072–1077.
- MACHADO, A., BODIGUEL, H., BEAUMONT, J., CLISSON, G. & COLIN, A. 2016 Extra dissipation and flow uniformization due to elastic instabilities of shear-thinning polymer solutions in model porous media. *Biomechanics* **10** (4), 043507.
- PRAT, M. 2007 On the influence of pore shape, contact angle and film flows on drying of capillary porous media. *International Journal of Heat and Mass Transfer* **50** (7), 1455–1468.
- PRAT, M. 2011 Pore network models of drying, contact angle, and film flows. *Chemical Engineering & Technology* **34** (7), 1029–1038.
- RAEINI, A. Q., BLUNT, M. J. & BIJELJIC, B. 2012 Modelling two-phase flow in porous media at the pore scale using the volume-of-fluid method. *Journal of Computational Physics* **231** (17), 5653–5668.
- RANSOHOFF, T. C. & RADKE, C. J. 1988 Laminar flow of a wetting liquid along the corners of a predominantly gas-occupied noncircular pore. *Journal of Colloid and Interface Science* **121** (2), 392–401.
- REID, R. C., PRAUSNITZ, J. M. & T. K., SHERWOOD 1987 *The properties of gases and liquids. 3rd Edition*. McGraw-Hill New York.
- SCHEEL, M., SEEMANN, R., BRINKMANN, M., DI MICHIEL, M., SHEPPARD, A., BREIDENBACH, B. & HERMINGHAUS, S. 2008a Morphological clues to wet granular pile stability. *Nature Materials* **7** (3), 189–193.
- SCHEEL, M., SEEMANN, R., BRINKMANN, M., DI MICHIEL, M., SHEPPARD, A. & HERMINGHAUS, S. 2008b Liquid distribution and cohesion in wet granular assemblies beyond the capillary bridge regime. *Journal of Physics: Condensed Matter* **20** (49), 494236.
- SCHERER, G. W. 1990 Theory of drying. *Journal of the American Ceramic Society* **73** (1), 3–14.

- SHAHIDZADEH-BONN, N., AZOUNI, A. & COUSSOT, P. 2007 Effect of wetting properties on the kinetics of drying of porous media. *Journal of Physics: Condensed Matter* **19** (11), 112101.
- SHAW, T.M. 1987 Drying as an immiscible displacement process with fluid counterflow. *Physical Review Letters* **59** (15), 1671.
- SHERWOOD, T. K. 1929*a* The drying of solidsi. *Industrial & Engineering Chemistry* **21** (1), 12–16.
- SHERWOOD, T. K. 1929*b* The drying of solidsii. *Industrial & Engineering Chemistry* **21** (10), 976–980.
- SHOKRI, N., LEHMANN, P. & OR, D. 2010 Liquid-phase continuity and solute concentration dynamics during evaporation from porous media: Pore-scale processes near vaporization surface. *Physical Review E* **81** (4), 046308.
- SINGH, K., MENKE, H., ANDREW, M., LIN, Q., RAU, C., BLUNT, M. J. & BIJELJIC, B. 2017*a* Dynamics of snap-off and pore-filling events during two-phase fluid flow in permeable media. *Scientific Reports* **7**.
- SINGH, K., SCHOLL, H., BRINKMANN, M., DI MICHIEL, M., SCHEEL, M., HERMINGHAUS, S. & SEEMANN, R. 2017*b* The role of local instabilities in fluid invasion into permeable media. *Scientific Reports* **7**.
- TSIMPANOIANNIS, I. N., YORTSOS, Y. C., POULOU, S., KANELLOPOULOS, N. & STUBOS, A. K. 1999 Scaling theory of drying in porous media. *Physical Review E* **59** (4), 4353.
- VAN BRAKEL, J. 1980 Mass transfer in convective drying .
- VARGAFNIK, N. B. 1975 *Handbook of physical properties of liquids and gases-pure substances and mixtures*. Hemisphere Publishing Corporation, New York, NY.
- VORHAUER, N., WANG, Y. J., KARAGHANI, A., TSOTSAS, E. & PRAT, M. 2015 Drying with formation of capillary rings in a model porous medium. *Transport in Porous Media* **110** (2), 197–223.
- YANG, F., GRIFFA, M., BONNIN, A., MOKSO, R., BELLA, C., MÜNCH, B., KAUFMANN, R. & LURA, P. 2015 Visualization of water drying in porous materials by x-ray phase contrast imaging. *Journal of Microscopy* **261** (1), 88–104.
- YIOTIS, A.G., SALIN, D., TAJER, E.S. & YORTSOS, Y.C. 2012*a* Analytical solutions of drying in porous media for gravity-stabilized fronts. *Physical Review E* **85** (4), 046308.
- YIOTIS, A.G., SALIN, D., TAJER, E. S. & YORTSOS, Y. C. 2012*b* Drying in porous media with gravity-stabilized fronts: Experimental results. *Physical Review E* **86** (2), 026310.
- YIOTIS, A. G., BOUDOUVIS, A. G., STUBOS, A. K., TSIMPANOIANNIS, I. N. & YORTSOS, Y. C. 2003 Effect of liquid films on the isothermal drying of porous media. *Physical Review E* **68** (3), 037303.
- YIOTIS, A. G., BOUDOUVIS, A. G., STUBOS, A. K., TSIMPANOIANNIS, I. N. & YORTSOS, Y. C. 2004 Effect of liquid films on the drying of porous media. *AIChE Journal* **50** (11), 2721–2737.